A Coupling Mechanism With Multidegree Freedom for Bidirectional Multistage WPT System

Jinde Wu, Xin Dai, *Member, IEEE*, Ruozhong Gao, and Jincheng Jiang

***Abstract*—For the application of wireless power transfer (WPT) technology in robot arm, it is necessary to provide flexible power supply for each arm device across multiple arm joints. However, rotation of the joints and the variation of the loads will lead to the fluctuation of the output voltage at each stage. To guarantee stable output voltage, a bidirectional multistage WPT (BM-WPT) method is proposed to provide energy for multiple loads. A bowl-coupling structure and three-dimensional orthogonal ring coil arrangement are proposed to reduce coupling variation against joint rotation. With a special resonant topology design for each stage, energy can be injected or output freely on each stage regardless of energy transfer direction. This topology can also reduce the sensitivity of the output voltages with the variation of the loads. The simulation and experimental results have verified the effectiveness of the proposed method and the coupling mechanism.**

***Index Terms*—Bidirectional, coupling mechanism, multidegree freedom, multistage, wireless power transfer (WPT).**

NOMENCLATURE

E_i	Input voltage of Stage *i*.
$Uac_{(i)}$	Output voltage of the inverter in Stage *i*.
R_i	Load of Stage *i*.
$S_{i1}, S_{i2}, S_{i3}, S_{i4}$	Driving signal of the inverter in Stage *i*.
C_i	Filter capacitor of Stage *i*.
$L_{p(i)1}, C_{p(i)1}, C_{p(i)2}, C_{s(i-1)}$	Compensation inductance and capacitances of Stage *i*.
$L_{p(i)2}, L_{si}$	Primary and secondary coils of Joint *i*.
$R_{p(i)2}, R_{si}$	Resistances of the primary and secondary coils in Joint *i*.
f, *w*	Operation frequency and angle frequency.
$U_{fo(i)}, U_{to(i)}$	Output voltage when the power is transferred in both directions.
P_{f_out}, P_{t_out}	Output power when the power is transferred in both directions.
$M_{rm(i)}$	Equivalent mutual inductance of Joint *i*.
M_{i1}, M_{i2}, M_{i3}	Mutual inductance between the primary coil and the three secondary coils of Joint *i*, respectively.
$L_{s(i)1}, L_{s(i)2}, L_{s(i)3}$	Self-inductances of three secondary coils in Joint *i*, respectively.
θ	Rotation angle of the secondary coil.
A, B, C	Area of Coil A, Coil B, and Coil C (three secondary coils), respectively.
S	Effective area of the secondary coil on the magnetic field orientation.
η	Efficiency of the system.

I. INTRODUCTION

FOR robot applications, wireless power transfer (WPT) technology provides a flexible and convenient method for power supply by utilizing high-frequency magnetic coupling [1]–[10]. Most WPT robot applications are designed to provide a robot battery charging method. However, there is an increasing demand for wireless power transmission across robot arm joints to provide power for driving machines mounted on the arms. It provides great benefits for robot arm design for the following aspects: 1) no risks of corrosion, twisting, or damage due to insulation; and 2) more flexibility and robustness for robot-arm-joint rotation. However, there exist some challenges for application of WPT technology in robot arms, including: 1) coupling-mechanism design difficulty because mutual coupling varies dramatically in robot arm rotation with multidegree freedom; 2) power transmission stability with the condition that multiple loads require energy; 3) bidirectional power transmission demand along robot arms.

There are few papers that discuss WPT applications for robot arms, but there are some relevant papers about WPT through the repeater unit. It is well known that the magnetic field and power transfer efficiency decrease rapidly with the increase of distance in WPT systems. Therefore, various methods have been

Manuscript received March 7, 2020; revised June 11, 2020; accepted July 9, 2020. Date of publication July 21, 2020; date of current version September 22, 2020. This work was supported by the National Natural Science Foundation of China under Grant 51777022. Recommended for publication by Associate Editor J. M. Rivas Davila. *(Corresponding author: Xin Dai.)*

The authors are with the School of Automation, Chongqing University, Chongqing 400044, China (e-mail: 376492330@qq.com; toybear@vip.sina.com; 782452614@qq.com; 704020211@qq.com).

Digital Object Identifier 10.1109/TPEL.2020.3010955

proposed to improve the transfer distance: a wired three-coil repeater is used to extend the distance and area [11], and the efficiency and transfer distance of a system are improved by optimizing the repeater coil [12]. Motoki and Atsushi [13] propose a system that not only transfers power far but also enables the receiver to move flexibly, which is achieved by a two-coil wired repeater. One repeater coil is coupled with the primary coil, and the other is coupled with the pickup coil, so the pickup coil and its coupled repeater coil can move freely. In addition to extending the transmission distance, Kittisak *et al.* [14] proposes a method that also expands the transmission range. Zhao *et al.* [15] present a system that the path of power flow is changed by the device with vector control technology. To select and enhance the power flow in WPT systems with multiple receivers, Zhong and Hui [16] designs auxiliary circuits that are used in receiver circuits to ensure wireless power flow to the targeted receivers. Above research works mainly focus on extension of energy transmission distance in systems with multiple repeater units. Therefore, the power transfer capability is a major concern, and the demand of robot arm application for power output capability on each repeater unit has not been taken into account.

Power transfer efficiency and transferred power are the key performance to be considered in WPT systems. Minh *et al.* [17]–[18] propose a method that improves the power transfer efficiency by using repeater resonators. To minimize the loss in both the power supply and the output stage, Wenxing *et al.* [19] designs a WPT system with a relatively low operating frequency. Sampath *et al.* [20] present an optimized method that improves both power transfer efficiency and transferred power against load variations. Masataka *et al.* [21] adopt an automatic tuning assist circuit in the repeater that can improve the robustness of the WPT system. Masataka *et al.* [22]–[23] propose a impedance matching method that can maximize the induced current in the repeater regardless of the variations of the magnetic coupling and the natural resonance frequency. Luo *et al.* [24] propose a flexible design method with any number of repeaters for WPT systems. Dai *et al.* [25] present a maximum efficiency tracking method that can satisfy the requirements of adaption for coupling coefficient and load variation, and output controllability. Current researches focus on output power and the improvement of system efficiency by optimizing coils and parameters. However, these methods could not be utilized in robot arm system because neither the variation of mutual inductance nor the multiload output along the power transmission chain is taken into account.

Ruiz *et al.* [26]–[28] study the application of bidirectional WPT system in high frequency. Ruiz *et al.* [26] propose a 915-MHz gallium nitride (GaN) high electron mobility transistor (HEMT)-based class-E rectifier. It can be used for dc+ac wireless power recovery. Taking the advantage of the time reversal duality principle, the efficiency of the system is improved and the sensitivity of the output network to load variation is reduced. Reveyrand *et al.* [27] discuss the similarity between radio frequency (RF) power amplifiers and rectifiers. With time-reversal duality, high efficiency is achieved in both operation modes. Del Prete *et al.* [28] present a battery-less bidirectional 2.45-GHz circuit. When it is operating in oscillator mode, it can be a power transmitter, while in rectifier mode, it can be an energy receiver. However, the above systems can only satisfy the requirement of bidirectional power transmission, while they are not designed for multistage power transmission.

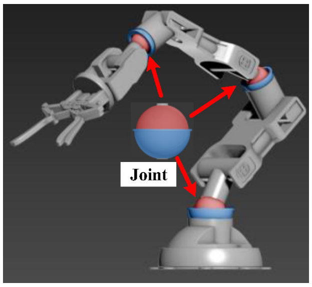

Fig. 1. BM-WPT system.

Pacini *et al.* [29] present a tiny, omnidirectional 13.56-MHz WPT system that is suitable for implantable applications. The system pays specific attention to miniaturization and omnidirectional capabilities. However, it is difficult to transfer power reversely, because more converters should be added in the system to satisfy reverse power transfer requirement. Due to parallel connection topology is adopted in the secondary side, it is difficult to choose which coil to transfer power reversely.

Aiming at multiple power output on repeater units, Cheng *et al.* [30] designs a resonant compensation topology for each repeater. The repeater units can transmit power to the loads connected to them, and then to the subsequent repeater unit. With the proposed compensation topology and an interleaving slice-type coil design, the load currents are independent of the loads. However, the system proposed in [30] cannot satisfy the requirement of bidirectional power transmission. Because under the condition of reverse power transmission, the system cannot ensure load-independent characteristic. In addition, as this method is not designed for rotation application with multidegree freedom, the slice-type repeater coils have to be placed on a straight direction.

Aiming at robot arm application, a coupling mechanism with multidegree freedom and bidirectional transmission capability is proposed to make it suitable for robot arm joint application. The bowl-coupling structure and three-dimensional (3-D) orthogonal ring coil arrangement are proposed. The coupling mechanism can achieve stable mutual inductance when it rotates. With a special resonant topology design for each stage, energy can be injected or output freely on each stage. This topology can guarantee that the output voltage is independent of load variation. This method provides a more flexible implementation method of multistage WPT system, which is adaptive for the driving of multiple machines on multiple arms.

II. PROPOSED BIDIRECTIONAL MULTISTAGE (BM)-WPT SYSTEM

Fig. 1 shows the BM-WPT system that is mainly applied on the robot arm. Each joint consists of a primary coil of the preceding stage and a secondary coil of the subsequent stage.

The circuit topology of the proposed BM-WPT system is presented in Fig. 2. There are $n + 1$ stages in the system,

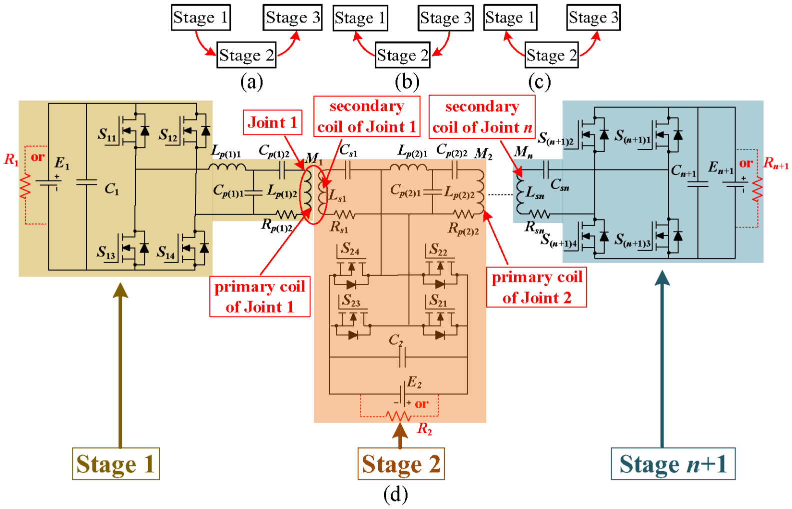

Fig. 2. Operation modes and the schematic diagram of the proposed BM-WPT system. (a) Forward power transmission. (b) Reverse power transmission. (c) Bidirectional power transmission. (d) Schematic diagram of the proposed BM-WPT system.

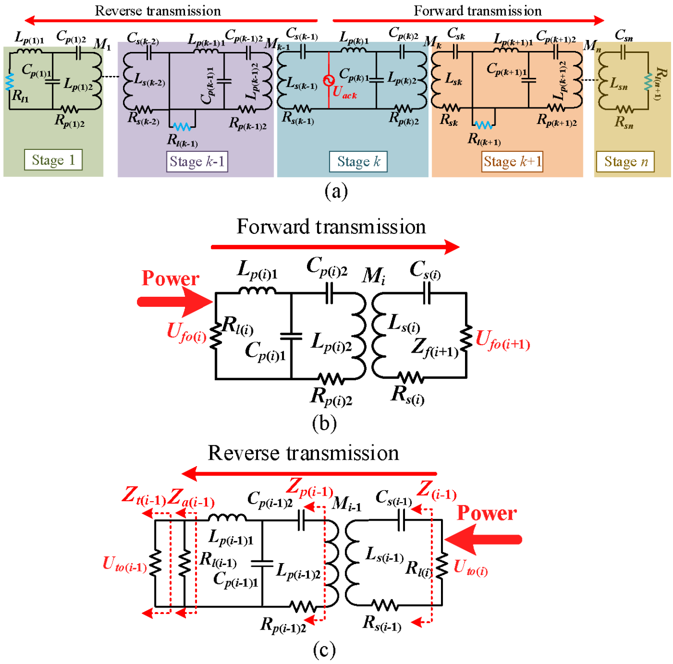

Fig. 3. Equivalent circuit of the system. (a) Simplified circuit of the system. (b) Forward power transmission. (c) Reverse power transmission.

which can be divided into three categories. *LCC* topology ($L_{p(1)1}$-$C_{p(1)1}$-$C_{p(1)2}$-$L_{p(1)2}$) is adopted in the Stage 1, *LC* series topology (L_{sn}-C_{sn}) is adopted in the Stage $n+1$, and all the other stages (from Stage 2 to Stage n) adopt both topologies ($L_{p(i)1}$-$C_{p(i)1}$-$C_{p(i)2}$-$L_{p(i)2}$ and $L_{s(i\text{-}1)}$-$C_{s(i\text{-}1)}$). Except Stage 1 and Stage $n+1$, there are two coils in the other stages, where the secondary coil is coupling with the primary coil of the preceding stage, and the primary coil is coupling with the secondary coil of the subsequent stage. The power can be injected or output from any stage. When the power is injected from Stage 1, it can be transferred in the forward direction. When the power is injected from Stage $n+1$, it can be transferred in the reverse direction. When the power is injected from other stages, it can be transferred in both directions. It can be seen that each stage includes power source (or load), high-frequency full-bridge converter, and resonance compensation network. There are two modes in each stage: energy receiving and energy transmitting. When the load receives energy, the converter works as a rectifier and the energy is transmitted to the load through rectifier and filter. In contrast, when the power source transmits energy, the converter works as an inverter, and the energy is transmitted to the resonance compensation network through the inverter.

Typical converters include full-bridge converter, half-bridge converter, and push–pull converter. Compared with half-bridge converter, full-bridge converter has higher output voltage gain. In the proposed bidirectional multistage WPT system, due to each stage must satisfy the requirement of bidirectional power flow, the converter works as the inverter or rectifier, while push–pull converter cannot satisfy bidirectional operation. Furthermore, the two splitting inductors used in the push–pull are bulky, which will reduce the power density of the system. So full-bridge converter is adopted in the system.

In the BM-WPT system, the voltage of the power source is expressed as E_i. A high-frequency full-bridge inverter working at a fixed frequency is utilized to produce a square-wave voltage source for the following resonant tanks. The energy is transmitted to each load through the resonance networks. In order to analyze the system, some fundamental definitions are proposed as follows: the resistances of each primary coil and each secondary coil are expressed as $R_{p(i)2}$ and $R_{s(i)}$, the mutual inductance is expressed as M_i, and the relationship between the dc voltage E_i and the inverter output voltage $U_{ac(i)}$ is

$$U_{\mathrm{ac}(i)} = \frac{2\sqrt{2}E_i}{\pi}\,(i = 1, 2\ldots n)\,. \tag{1}$$

When the loads receive energy, the ac equivalent impedance of each load is $R_{l(i)} = 8R_i/\pi^2$ ($i = 1, 2\ldots n$).

TABLE I
FORWARD TRANSMISSION

The relationship between the output voltage of Stage i and Stage i+1	$\dot{U}_{fo(i+1)} = \dfrac{\dot{U}_{fo(i)} M_i Z_{f(i+1)}}{L_{p(i)}\left(Z_{f(i+1)} + R_{s(i)}\right)} (i = k+1, k+2 \ldots n)$
Output power	$P_{f\_out} = \sum_{i=k+1}^{n+1} \dfrac{U_{fo(i)}^2}{R_{l(i)}}$

TABLE II
REVERSE TRANSMISSION

The relationship between the output voltage of Stage i and Stage i-1	$\dot{U}_{to(i-1)} = \dfrac{\dot{U}_{to(i)}\, \omega^2 M_{i-1} L_{p(i-1)} Z_{a(i-1)}}{\left(\omega M_{i-1}\right)^2 Z_{a(i-1)} + R_{s(i-1)}\left(\left(\omega L_{p(i-1)}\right)^2 + R_{p(i-1)2} Z_{a(i-1)}\right)}$ $(i = 2, 3 \ldots k\text{-}1)$
Output power	$P_{t\_out} = \sum_{i=1}^{k\text{-}1} \dfrac{U_{to(i)}^2}{R_{l(i)}}$

If (2) is satisfied, the equivalent impedances of all resonant networks will exhibit resistive

$$\begin{cases} \omega^2 = \frac{1}{L_{p(i)} C_{p(i)1}} = \frac{1}{L_{p(i)1} C_{p(i)1}} = \frac{1}{L_{s(i)} C_{s(i)}} \\ \frac{1}{j\omega C_{p(i)2}} + j\omega L_{p(i)2} = j\omega L_{p(i)}. \end{cases}, \ (i = 1, 2 \ldots n) \tag{2}$$

III. MODELING OF THE BM-WPT SYSTEM

The equivalent circuit of the system is shown in Fig. 3. When the power source U_{ack} transmits energy, the energy is transmitted to the loads in both forward and reverse directions through the resonance compensation network. The output voltage and the output power of each stage are shown in Tables I and II. When the power is transmitted forward, the output voltage is expressed as $U_{fo(i)}$, and when the power is transmitted in reverse, the output voltage is expressed as $U_{to(i)}$.

According to Fig. 3 (b), $Z_{f(i+1)}$ is the total impedance after the Stage i. In Table I, $Z_{f(i+1)}$ and $Z_{f(n+1)}$ can be expressed as follows:

$$Z_{f(i+1)} = \frac{\left(\omega L_{p(i+1)}\right)^2 \left(Z_{f(i+2)} + R_{s(i+1)}\right)}{\left(\omega M_{i+1}\right)^2 + R_{p(i+1)2}\left(Z_{f(i+2)} + R_{s(i+1)}\right)} // R_{l(i+1)} \ (i = k, k+1 \ldots n-1) \tag{3}$$

$$Z_{f(n+1)} = R_{l(n+1)}. \tag{4}$$

According to Fig. 3 (c), $Z_{a(i-1)}$ is the total impedance before the Stage i. In Table II, $Z_{t(i-1)}$, $Z_{a(i-1)}$ and $Z_{a(1)}$ can be expressed as follows:

$$Z_{t(i-1)} = R_{s(i-2)} + \frac{\left(\omega M_{i-2}\right)^2 Z_{a(i-2)}}{\left(\omega L_{p(i-2)}\right)^2 + R_{p(i-2)2} Z_{a(i-2)}}, \times (i = 3, 4 \ldots k) \tag{5}$$

$$Z_{a(i-1)} = Z_{t(i-1)} // R_{l(i-1)}, \ (i = 3, 4 \ldots k) \tag{6}$$

$$Z_{a(1)} = R_{l(1)}. \tag{7}$$

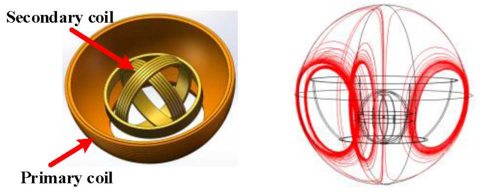

(a) (b)

Fig. 4. Design of the coupling mechanism. (a) Structure of the coupling mechanism. (b) Magnetic field of the coupling mechanism.

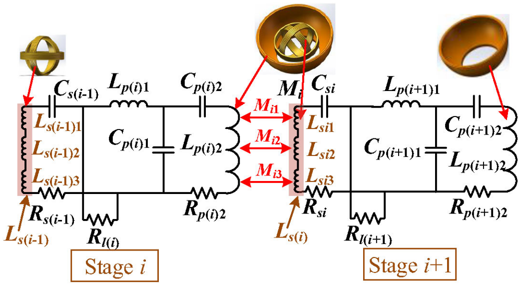

Fig. 5. Coupling between the primary coil and the secondary coil.

IV. DESIGN OF THE COUPLING MECHANISM WITH MULTIDEGREE FREEDOM

In the robot arm application, the mutual inductance between the primary and secondary coils will vary with the rotation of the joints. Therefore, to maintain the stability of the output voltage of each stage, the sensitivity of the mutual inductance to the dynamical rotation of the joints is supposed to be reduced. Based on the above discussion, the bowl-coupling structure and 3-D orthogonal ring coil arrangement with multidegree freedom are proposed in Fig. 4.

It can be seen from Fig. 4 that the primary coil is designed as a bowl structure, and the secondary coil is designed as a 3-D orthogonal ring coil arrangement. Fig. 5 shows the coupling between the primary coil and the secondary coil. The variation of the mutual inductance with the rotation angle of the secondary coil is analyzed through theory and simulation. Three secondary coils are vertical to each other and the cross mutual inductance among them is zero. $L_{s(i\text{-}1)}$ is composed of $L_{s(i\text{-}1)1}$, $L_{s(i\text{-}1)2}$, and $L_{s(i\text{-}1)3}$ in series, and $L_{s(i)}$ is composed of $L_{s(i)1}$, $L_{s(i)2}$, and $L_{s(i)3}$ in series.

Fig. 5 indicates that the equivalent mutual inductance $M_{rm(i)}$ at each stage can be expressed as follows:

$$M_{rm(i)} = \left|M_{i1} + M_{i2} + M_{i3}\right|. \tag{8}$$

Fig. 6 illustrates the rotation direction of the secondary coils and the reference direction of the secondary coils connecting. The three coils in the *XY*, *XZ*, and *YZ* planes are marked as Coil A, Coil B, and Coil C, respectively. When three orthogonal secondary coils are connected clockwise, the reference direction is positive and marked with "+" [it is marked in Fig. 6(a)], otherwise it is negative and marked with "−". Fig. 6 indicates that when the secondary coil rotates in the *XY* plane, Coil A does

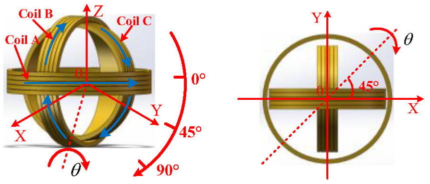

(a) (b)

Fig. 6. Rotation direction of the secondary coil and the reference direction of the secondary coils connecting. (a) General view of the secondary coil. (b) Top view of the secondary coil.

TABLE III
RESULTS OF THE COMSOL SIMULATION

Secondary coils			M_{rm} (μH)						
A	B	C	θ=0°	15°	30°	45°	60°	75°	90°
+	+	+	2.93	1.94	0.86	0.21	1.23	2.13	2.82
+	+	-	2.93	2.70	2.27	1.68	0.98	0.18	0.57
+	-	+	2.93	2.96	2.73	2.30	1.67	0.92	0.15
+	-	-	2.93	3.68	4.14	4.29	4.06	3.63	2.92
-	+	+	2.93	3.68	4.14	4.29	4.06	3.63	2.92
-	+	-	2.93	2.96	2.73	2.30	1.67	0.92	0.15
-	-	+	2.93	1.94	0.86	0.21	1.23	2.13	2.82
-	-	-	2.93	1.94	0.86	0.21	1.23	2.13	2.82

not change with the magnetic field orientation generated by the primary coil, and as a result the mutual inductance between them does not change. In addition, the primary coil is vertical to the other two secondary coils, Coil B and Coil C, respectively, and the mutual inductance between the primary coil and Coil B, as well as that between the primary coil and Coil C are both zero. According to (8), when the secondary coil rotates in the *XY* plane, $M_{rm(i)}$ does not vary and it is just the mutual inductance between the primary coil and Coil A. Therefore, we need to focus on the mutual inductance fluctuation when the secondary coil rotates in the *XZ* and *YZ* planes.

The first and third quadrant angular bisectors of *XY* plane are selected as the rotation axis for research (as shown in Fig. 6). The rotation angle is recorded as θ. Because the magnetic field orientation generated by the primary coil is vertical to the *XY* plane, the effective area of the secondary coil in the magnetic field direction is projected on the *XY* plane. If the areas of Coil A, Coil B, and Coil C are recorded as A, B, and C respectively, the effective area *S* during the rotation of the secondary coil can be expressed as follows:

$$\begin{aligned} S &= A\cos\theta + B\cos 45^\circ \sin\theta + C\cos 45^\circ \sin\theta \\ &= \sqrt{A^2 + \frac{(B+C)^2}{2}}\sin(\theta+\varphi) \end{aligned} \tag{9}$$

where the relationship between φ and the area of Coil A, Coil B, and Coil C is expressed as

$$\varphi = \arctan\left(\frac{\sqrt{2}A}{B+C}\right). \tag{10}$$

The derivative of the rotation angle θ can be obtained from (9)

$$\frac{dS}{d\theta} = \sqrt{A^2 + \frac{(B+C)^2}{2}}\cos(\theta+\varphi). \tag{11}$$

Equation (11) indicates that when θ varies from 0 to π-2φ, d*S*/dθ undergoes a corresponding variation from 0 to the peak value and then to 0 again. d*S*/dθ approaches the peak value when θ approaches π/2-φ, which indicates that the effective area of the secondary coil and $M_{rm(i)}$ reach the maximum, and the minimum values occur at $\theta = 0$ and $\theta = \pi$-2φ. If the rotation angle of the secondary coil is θ∈[0, γ], to reduce the fluctuation of $M_{rm(i)}$ with θ, then

$$\frac{\pi}{2} - \varphi = \frac{\gamma}{2} \tag{12}$$

$$\varphi = \frac{\pi - \gamma}{2}. \tag{13}$$

The effective area of the secondary coil is the maximum at $\theta = \gamma/2$ and the minimum at $\theta = 0$ and $\theta = \gamma$. The ratio of the maximum $S_{\max}$ and the minimum $S_{\min}$ of area is

$$T = \frac{S_{\max}\left(\frac{\gamma}{2}\right)}{S_{\min}(0)} = \frac{S_{\max}\left(\frac{\gamma}{2}\right)}{S_{\min}(\gamma)} = \frac{1}{\sin\left(\frac{\pi-\gamma}{2}\right)}. \tag{14}$$

This is also the ratio of the maximum and the minimum of $M_{rm(i)}$. In the application of robot arm, if the secondary coil rotates 90°, then $\gamma = 90^\circ$, $\varphi = 45^\circ$, and then

$$\tan\varphi = \tan 45^\circ = \frac{\sqrt{2}A}{B+C} = 1. \tag{15}$$

If $B = k_1A$, $C = k_2A$, then

$$k_1 + k_2 = \sqrt{2}. \tag{16}$$

Magnetic field analysis is carried out on the coupling mechanism with COMSOL software, and the area of the secondary coil satisfies (16). According to the COMSOL simulation, when the secondary coils rotate clockwise along the angle bisector of the first and third quadrants of the *XY* plane, the simulation results of different connecting methods are listed in the Table III, and the variation of the equivalent mutual inductance M_{rm} with θ is shown in the Fig. 7.

It can be seen from Table III and Fig. 7, when "$+--$" or "$-++$" is selected as the connecting method of the three secondary coils, the fluctuation of the equivalent mutual inductance M_{rm} with the rotation angle θ is small. So "$+--$" or "$-++$" (highlight in Table III) is adopted in the system. It can be seen in Fig. 7 that $M_{rm(i)}$ undergoes a corresponding variation from the minimum to the peak value and then to the minimum again. When $\theta = 45^\circ$, $M_{rm(i)}$ reaches the top; when $\theta = 90^\circ$, $M_{rm(i)}$ reaches the bottom. The ratio of the maximum and the minimum is

$$\frac{M_{rm\max}}{M_{rm\min}} = \frac{4.29}{2.93} = 1.46 \approx \sqrt{2}. \tag{17}$$

V. OUTPUT CHARACTERISTIC ANALYSIS

With the design of the above coupling mechanism, the mutual inductance variation can be reduced. On the basis, the output

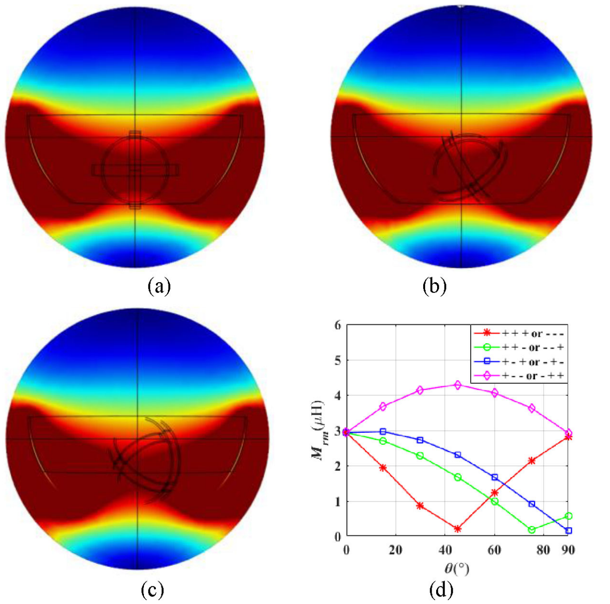

Fig. 7. Magnetic field simulation of the proposed bowl-structure coupling mechanism. (a) $\theta = 0°$, (b) $\theta = 45°$, (c) $\theta = 90°$, and (d) variation of M_{rm} with θ.

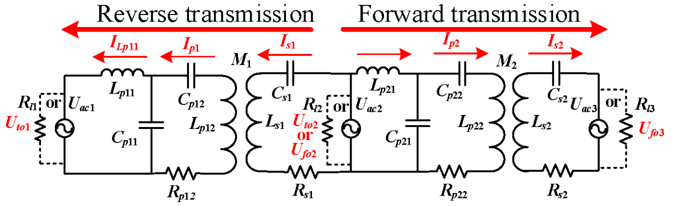

Fig. 8. Model of the simulation and experiment.

characteristic analysis should be given to guarantee that each stage has similar and steady output performance. A three-stage BM-WPT system is taken as an example to analyze the influence of the loads and the rotation angles of the secondary coils. The model of the system is shown in Fig. 8.

When the system is powered by E_2, R_{l1} and R_{l3} are used to receive energy, and the analysis and results of simulation are as follows. The rotation angles of the secondary coils on the Joint 1 and the Joint 2 are expressed as θ_1 and θ_2, respectively.

A. Analysis of the Output Voltages

Compared with the load, the resistance of the coil is small. If the resistance of the coil is ignored, when the power is transferred in the forward direction, the output voltage at each stage is

$$\dot{U}_{fo(i)} = \frac{\dot{U}_{ac(k)} M_k M_{k+1} \ldots M_{i-1}}{L_{p(k)} L_{p(k+1)} \ldots L_{p(i-1)}} \quad (i = k+1, k+1 \ldots n+1). \tag{18}$$

When the power is transmitted reversely, according to Fig. 3(c), $Z_{a(i-1)}$ is the total impedance before the Stage i. The impedance $Z_{p(i-1)}$ can be expressed as

$$Z_{p(i-1)} = \frac{\left(\omega L_{p(i-1)}\right)^2}{Z_{a(i-1)}}. \tag{19}$$

The total impedance $Z_{(i\text{-}1)}$ can be expressed as

$$Z_{(i-1)} = R_{s(i-1)} + \frac{\left(\omega M_{i-1}\right)^2}{Z_{p(i-1)} + R_{p(i-1)2}}. \tag{20}$$

The induced voltage $U_{p(i\text{-}1)}$ of the coil $L_{p(i\text{-}1)2}$ is

$$\dot{U}_{p(i-1)} = \frac{\omega M_{i-1} \dot{U}_{to(i)}}{Z_{(i-1)}}. \tag{21}$$

The output voltage $U_{to(i\text{-}1)}$ can be expressed as

$$\begin{aligned} \dot{U}_{to(i-1)} &= \frac{\dot{U}_{p(i-1)} Z_{p(i-1)} Z_{a(i-1)}}{\left(Z_{p(i-1)} + R_{p(i-1)2}\right) \omega L_{p(i-1)}} \\ &= \frac{\dot{U}_{to(i)} \omega^2 M_{i-1} L_{p(i-1)} Z_{a(i-1)}}{\left(\omega M_{i-1}\right)^2 Z_{a(i-1)} + R_{s(i-1)} \left(\left(\omega L_{p(i-1)}\right)^2 + R_{p(i-1)2} Z_{a(i-1)}\right)}. \end{aligned} \tag{22}$$

If the resistances of the coils are ignored, (22) can be simplified as

$$\dot{U}_{to(i-1)} = \frac{\dot{U}_{to(i)} L_{p(i-1)}}{M_{i-1}}. \tag{23}$$

Therefore, if the power is injected from Stage k, the output voltage at each stage in the reverse direction can be expressed as

$$\dot{U}_{to(i)} = \frac{\dot{U}_{ac(k)} L_{p(k-1)} L_{p(k-2)} \ldots L_{p(i)}}{M_{k-1} M_{k-2} \ldots M_i} \quad (i = 1, 2 \ldots k-1). \tag{24}$$

Based on (18) and (24), the output voltages are independent of the loads. The variations of the output voltages with the loads and the rotation angles of the secondary coils are shown in Fig. 9.

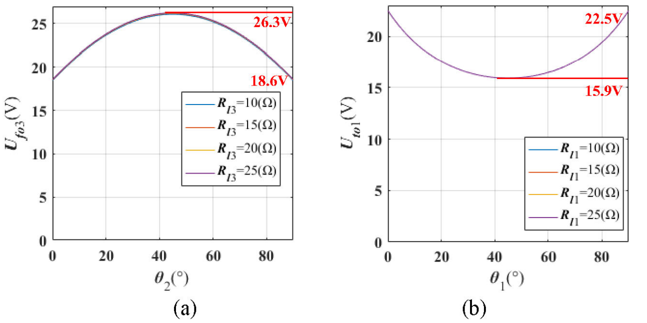

Fig. 9. Variations of the output voltages with the loads and the rotation angles of the secondary coils. (a) Forward transmission. (b) Reverse transmission.

Fig. 9 indicates that the output voltages are independent of the loads regardless of the direction in which the energy is transmitted. If the energy is transmitted forward, when θ_1 is fixed at 45°, the output voltage U_{fo3} varies from the minimum 18.6 V to the peak value 26.3 V and returns to the minimum 18.6 V when θ_2 increases from 0° to 90°. If the energy is transmitted

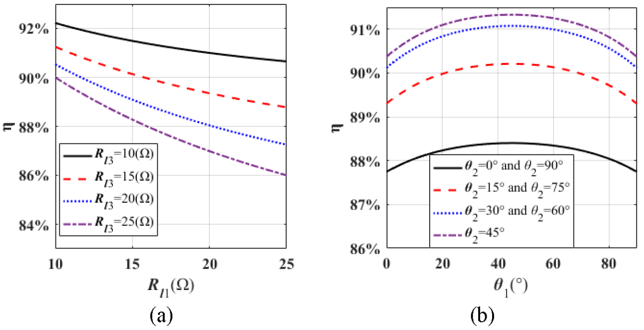

Fig. 10. Variations of the efficiency with the loads and the rotation angles of the secondary coils. (a) Variation of the efficiency with the loads. (b) Variation of the efficiency with the rotation angles of the secondary coils.

in reverse, when θ_2 is fixed at 45°, the output voltage U_{to1} varies from the maximum 22.5 V to the lowest value 15.9 V and returns to the maximum 22.5 V when θ_1 increases from 0° to 90°.

B. Analysis of the Efficiency

The efficiency of the simulation and experimental model can be expressed as (25), shown at the bottom of this page.

Variations of the efficiency with the loads and the rotation angles of the secondary coils are shown in Fig. 10. As can be seen in Fig. 10 (a), when both θ_1 and θ_2 are fixed at 0°, the efficiency decreases with the increase R_{l1} and R_{l3}, and its minimum is 86% and the maximum is 92.2%. Fig. 10 (b) depicts that when both R_{l1} and R_{l3} are fixed at 20 Ω, the efficiency varies from the minimum to the peak value and returns to the minimum with the increase of θ_1 and θ_2, and its minimum is 87.8% and the maximum is 91.3%. According to the simulation results in Fig. 10, the efficiency is larger than 86%. Where

$$a = \frac{\omega^2 M_1^2 R_{l1}}{\omega^2 L_{p(1)}^2 + R_{l1} R_{p(1)2}} + R_{s1} \tag{26}$$

$$b = \frac{\omega^2 L_{p(1)}^2}{R_{l1}} + R_{p(1)2}. \tag{27}$$

VI. Experimental Verification

To verify the proposed method, an experimental demonstration platform that was charging for robot arm is shown in Fig. 11. FPGA chip (EP2C5T144C8) was selected as the main control unit and MOSFET SiHG32N50D as the main switching components. The system consisted of three stages. *LCC* and *LC* topologies were adopted in the system. In the design of the experimental setup, the primary coils were bowl structure with a diameter of 100 mm, and the secondary coils were 3-D orthogonal ring coil arrangement. According to the above theoretical analysis, three rings of the secondary coils were designed with diameters of 60, 53.7, and 47.0 mm, respectively. The primary coils were wound 36 turns and the three rings of the secondary coils were wound 4 turns, respectively. The experimental parameters are shown in Table IV.

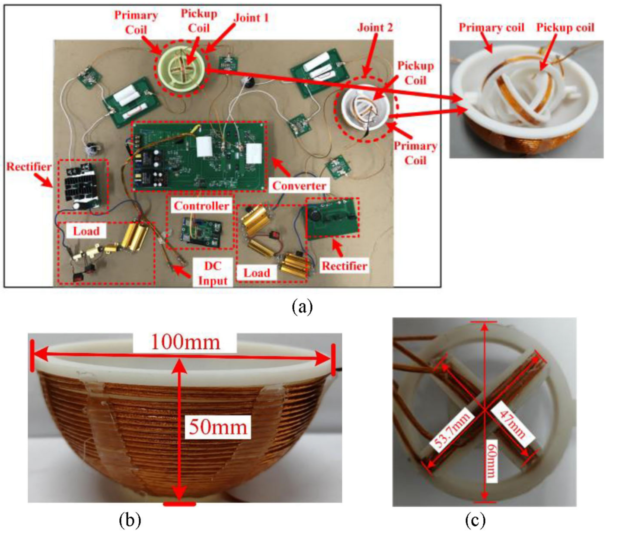

Fig. 11. Experimental setup and coupling mechanism. (a) Experimental setup, (b) primary coil, and (c) secondary coil.

TABLE IV
Experimental Parameters

Parameter	Value	Parameter	Value
E_1	20 V	E_2	22 V
E_3	25 V	f	150 kHz
$L_{p(1)1}$	3.925 μH	$C_{p(1)1}$	287 nF
$C_{p(1)2}$	18 nF	$L_{p(1)2}$	66.4 μH
$R_{p(1)2}$	0.201 Ω	L_{s1}	5.5μH
R_{s1}	0.01 Ω	C_{s1}	205 nF
$L_{p(2)1}$	4.2μH	$C_{p(2)1}$	268 nF
$C_{p(2)2}$	18.4 nF	$L_{p(2)2}$	65.24 μH
$R_{p(2)2}$	0.208 Ω	L_{s2}	5.5 μH
R_{s2}	0.01 Ω	C_{s2}	205 nF

The validity of the theory and the feasibility of the proposed system were verified based on the following three aspects.

1) The system was powered by E_2 with loads R_1 and R_3. The effects of θ_1, θ_2 and R_1, R_3 on U_{to1} and U_{fo3} were researched.
2) The system was powered by E_1 with loads R_2 and R_3. The effects of θ_1, θ_2 and R_2, R_3 on U_{fo2} and U_{fo3} were researched.
3) The system was powered by E_3 with loads R_1 and R_2. The effects of θ_1, θ_2 and R_1, R_2 on U_{to1} and U_{to2} were researched.
4) The circuit of the experimental model is shown in Fig. 8.

$$\eta = \frac{\omega^2\left(\omega^4 M_1^2 L_{p(1)}^2 L_{p(2)}^2 (R_{s2}+R_{l3})^2 + M_2^2 R_{l1} R_{l3} a^2 b^2\right)}{\left(\omega^6 M_1^2 L_{p(1)}^2 L_{p(2)}^2 (R_{s2}+R_{l3})^2 + \omega^4 M_1^2 R_{p(1)2} R_{l1} L_{p(2)}^2 (R_{s2}+R_{l3}) + \omega^2 b^2 R_{l1}\left(a^2 M_2^2 + R_{s1} L_{p(2)}^2 (R_{s2}+R_{l3})\right) + a^2 b^2 R_{p(2)2} R_{l1} (R_{s2}+R_{l3})\right)(R_{s2}+R_{l3})} \tag{25}$$

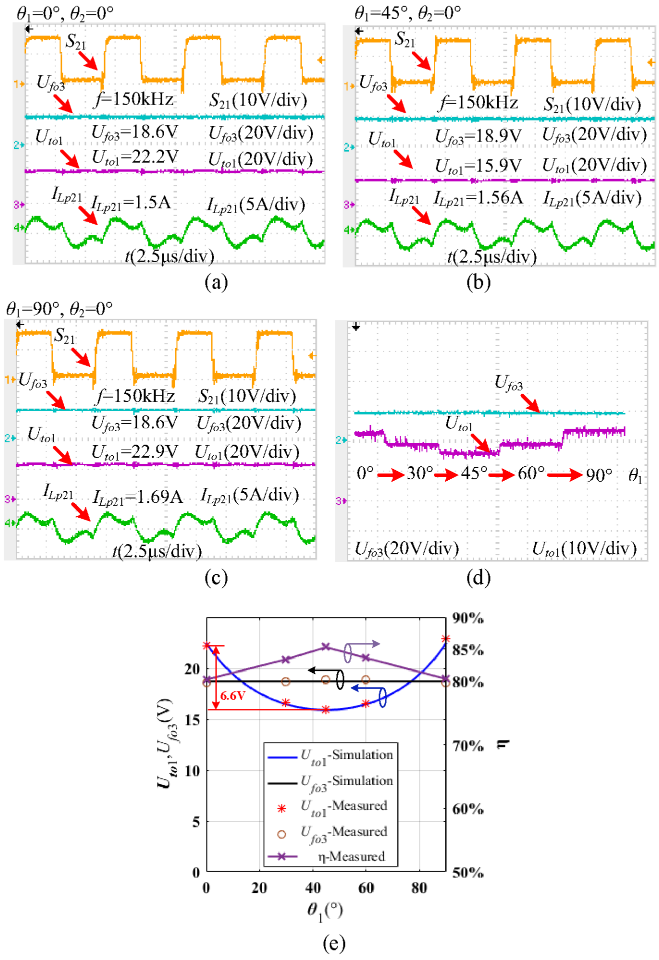

(a) (b) (c) (d) (e)

Fig. 12. Variations of the output voltages with θ_1 when $\theta_2 = 0°$, $R_1 = R_3 = 20\ \Omega$. (a) $\theta_1 = 0°$, (b) $\theta_1 = 45°$, (c) $\theta_1 = 90°$. (d) Variation of the output voltages with θ_1. (e) Comparison between the simulation and the experiment results.

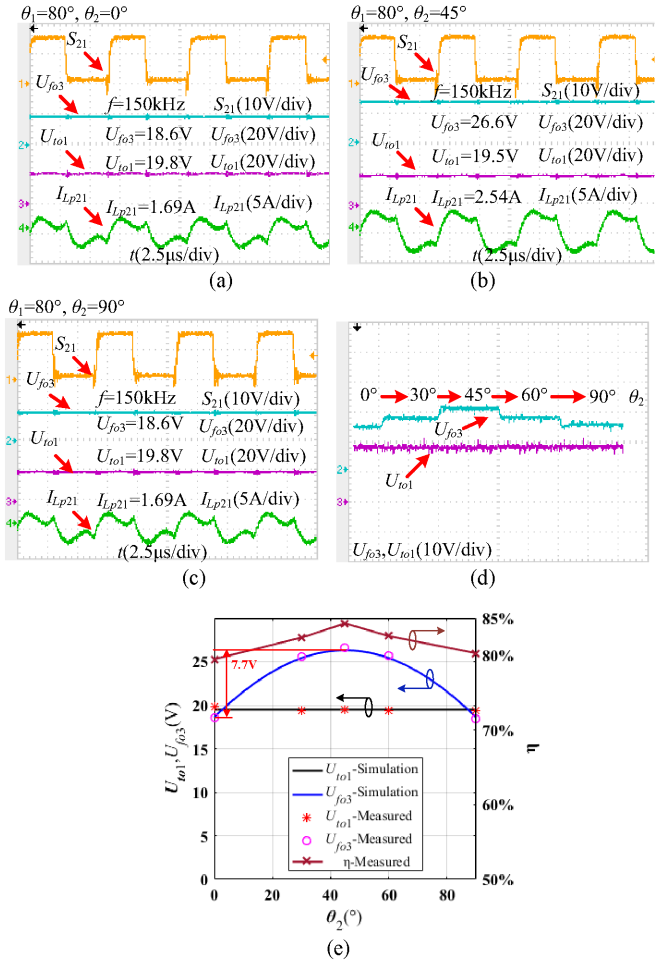

(a) (b) (c) (d) (e)

Fig. 13. Variations of the output voltages with θ_2 when $\theta_1 = 80°$, $R_1 = R_3 = 20\ \Omega$. (a) $\theta_2 = 0°$. (b) $\theta_2 = 45°$. (c) $\theta_2 = 90°$. (d) Variation of the output voltages with θ_2. (e) Comparison between the simulation and the experiment results.

TABLE V
VARIATION OF OUTPUT VOLTAGES AND TRANSFER POWER WITH LOADS

R_1 (Ω)	R_3 (Ω)	U_{to1} (V)	U_{fo3} (V)	Transfer power (W)	Efficiency
15	20	19.2	22.8	50.57	82.4%
20	15	19.9	22.1	52.36	85.1%
20	20	20.1	22.8	46.19	86.4%
20	25	19.9	23.5	41.89	86.1%
25	20	20.3	22.9	42.7	82.8%

A. E_2 as the Power Source, R_1 and R_3 as the Loads

1) Variation of U_{to1} and U_{fo3} With θ_1: The experimental results with E_2 as the power source, R_1 and R_3 as the loads are shown in Fig. 12, where $\theta_2 = 0°$, $R_1 = R_3 = 20\ \Omega$. Fig. 12(a)–(c) shows the driving signal of S_{21}, the current in the inductance L_{p21}, and the output voltages U_{to1} and U_{fo3} when θ_1 varied, and the dynamic process is shown in Fig. 12(d). The comparisons between the simulation results and the experiment results are shown in Fig. 12(e). Fig. 12(d) and (e) indicates that U_{fo3} varied slightly with the variation of θ_1. When $0° < \theta_1 < 45°$, U_{to1} decreased from 22.2 to 15.9 V with the increase of θ_1. When $45° < \theta_1 < 90°$, U_{to1} increased from 15.9 to 22.9 V with the increase of θ_1. According to (24), M_1 underwent a corresponding variation from the minimum to the peak value and then to the minimum again, and the maximum is 1.440 times the minimum. The efficiency varies from 80% to the peak value 85% and returns to the 80.2% with the increase of θ_1.

2) Variation of U_{to1} and U_{fo3} With θ_2: When E_2 was as power source, R_1 and R_3 were as loads ($R_1 = R_3 = 20\ \Omega$), $\theta_1 = 80°$ and θ_2 varied, the experimental results are shown in Fig. 13. Fig. 13(d) and (e) indicates that U_{to1} varied slightly with the variation of θ_2. When $0° < \theta_2 < 45°$, U_{fo3} increased from 18.6 to 26.6 V with the increase of θ_2. When $45° < \theta_2 < 90°$, U_{fo3} decreased from 26.6 to 18.6 V with the increase of θ_2. According to (18), M_2 underwent a corresponding variation from the minimum to the peak value and to the minimum again, and the maximum is 1.438 times the minimum. The efficiency varies from 80.1% to the peak value 84.8% and returns to 80.5% with the increase of θ_2.

3) Variation of U_{to1} and U_{fo3} With R_1 and R_3: When E_2 was used as power source, the output voltages varying with R_1 and R_3 are shown in Fig. 14 and Table V: $U_{to1\max} = 20.3$ V, $U_{to1\min} = 19.2$ V, $\Delta U_{to1} = 1.1$ V, $U_{fo3\max} = 23.5$ V, $U_{fo3\min} = 22.1$ V,

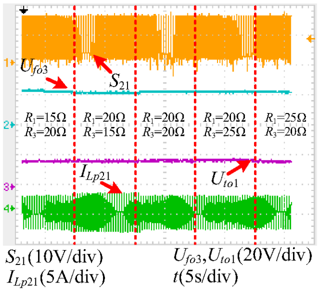

Fig. 14. Variations of the output voltages with the loads.

TABLE VI
VARIATION OF OUTPUT VOLTAGES AND TRANSFER POWER WITH θ_1 AND θ_2

θ_1 (°)	θ_2 (°)	U_{fo2} (V)	U_{fo3} (V)	Transfer Power (W)	Efficiency
0°	45°	18.1	25.8	50	81.3%
30°	0°	24	23.8	57.12	81.4%
30°	45°	24	33.8	85.92	84.0%
45°	90°	25.3	25	63.25	81.5%
90°	45°	18.5	26.4	51.96	80.5%

TABLE VII
VARIATION OF OUTPUT VOLTAGES AND TRANSFER POWER WITH LOADS

R_2 (Ω)	R_3 (Ω)	U_{fo2} (V)	U_{fo3} (V)	Transfer Power (W)	Efficiency
20	20	20.9	21.6	45.17	82.1%
25	20	21.8	21.9	42.99	80.4%
25	25	21.8	22.1	38.55	79.6%

TABLE VIII
VARIATION OF OUTPUT VOLTAGES AND TRANSFER POWER WITH θ_1 AND θ_2

θ_1 (°)	θ_2 (°)	U_{to1} (V)	U_{to2} (V)	Transfer Power (W)	Efficiency
0°	45°	16.5	17.2	28.40	80.1%
45°	0°	16.8	24.3	43.64	84.1%
90°	0°	23.7	24.4	57.85	83.3%
90°	45°	16.3	17.4	28.42	79.8%

TABLE IX
VARIATION OF OUTPUT VOLTAGES AND TRANSFER POWER WITH LOADS

R_1 (Ω)	R_2 (Ω)	U_{to1} (V)	U_{to2} (V)	Transfer Power (W)	Efficiency
15	15	19.7	20.1	52.81	88.7%
15	25	19.7	21.3	44.02	84.2%
20	15	20.3	20.1	47.54	85.0%
20	20	20.8	21.7	45.18	84.7%

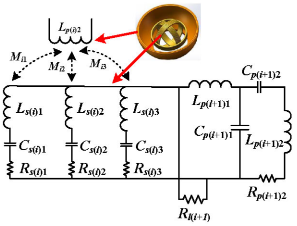

Fig. 15. Parallel connection of the secondary coils.

$\Delta U_{fo3} = 1.4$ V. The output voltages varied slightly with the variation of the loads, indicating that the output voltages were independent of the loads.

B. E_1 as the Power Source, R_2 and R_3 as the Loads

1) Variation of U_{fo2} and U_{fo3} With θ_1 and θ_2: When E_1 was used as power source, the output voltages varying with θ_1 and θ_2 are shown in Table VI. The loads of R_2 and R_3 were both 20 Ω. The inductance $L_{p(i)1}$ was designed to be equal to M_i when $\theta_i = 0°$ in the experimental system. According to (18), U_{fo3} increased with the increase of M_2. It can be seen in Table VI that $U_{fo3} > U_{fo2}$ when $\theta_2 > 0$ because M_2 was the minimum when $\theta_2 = 0$.

2) Variation of U_{fo2} and U_{fo3} With R_2 and R_3: When E_1 was used as power source, the output voltages varying with R_2 and R_3 are shown in Table VII: $U_{fo2\max} = 21.8$ V, $U_{fo2\min} = 20.9$ V, $\Delta U_{fo2} = 0.9$ V, $U_{fo3\max} = 22.1$ V, $U_{fo3\min} = 21.6$ V, $\Delta U_{fo3} = 0.5$ V. The output voltages varied slightly with the variation of the loads, which shows that the output voltages are independent of the loads.

C. E_3 as the Power Source, R_1 and R_2 as the Loads

1) Variation of U_{to1} and U_{to2} With θ_1 and θ_2: When E_3 was used as power source, the output voltages varying with θ_1 and θ_2 are shown in Table VIII. The load of R_1 and R_2 were 20 Ω. According to (24), U_{to1} decreased with the increase of M_1. It can be seen in Table VIII that $U_{to1} < U_{to2}$ when $\theta_1 > 0$ because M_1 was the minimum when $\theta_1 = 0$.

2) Variation of U_{to1} and U_{to2} With R*$_1$ and* R*$_2$:* When E_3 was used as power source, the output voltages varying with R_1 and R_2 are shown in Table IX: $U_{to1\max} = 20.8$ V, $U_{to1\min} = 19.7$ V, $\Delta U_{to1} = 1.1$ V, $U_{to2\max} = 21.7$ V, $U_{to2\min} = 20.1$ V, $\Delta U_{to2} = 1.6$ V. The output voltages varied slightly with the variation of the loads, which shows that the output voltages are independent of the loads.

Table X lists current research works on multistage WPT systems. Compared with previous works, proposed method in this article can realize dynamic rotation with multidegree freedom and satisfy multistage and bidirectional transmission requirements for robot arm application.

VII. DISCUSSION

A. Parallel Connection of the Secondary Coils

If the secondary coils are connected in parallel, the equivalent circuit is shown in Fig. 15.

According to Fig. 15, if (28) is satisfied, the equivalent impedances of the secondary side will exhibit resistive

$$\begin{cases} C_{s(i)1} = \frac{1}{\omega^2 L_{s(i)1}} \\ C_{s(i)2} = \frac{1}{\omega^2 L_{s(i)2}} \\ C_{s(i)3} = \frac{1}{\omega^2 L_{s(i)3}}. \end{cases} \quad (28)$$

When the secondary coils are dynamic rotation and the power is transferred forward, the mutual inductances between the primary coil and the three secondary coils are different. The induced voltages on the three secondary coils are also different.

TABLE X
COMPARISON OF RECENT WORKS ON MULTISTAGE WPT SYSTEMS

Paper	Number of repeaters	Whether the coil can dynamic rotate	Whether the repeater can output energy	Bi-directional transmission capability	Power level	Efficiency
[11]	1	None	NO	NO	2mW	71%
[12]	1	None	NO	NO	20W	55%
[13]	1	None	NO	NO	6mW	80%
[14]	1	None	NO	NO	3W	75%
[15]	n	None	NO	NO	123mW	Not Mentioned
[16]	n	None	NO	NO	5W	73.4%
[17]	n	20°	NO	NO	Not Mentioned	88%
[18]	n	None	NO	NO	Not Mentioned	46%
[19]	n	None	NO	NO	30W	80%
[20]	1	None	NO	NO	1W	90%
[21]	1	None	NO	NO	Not Mentioned	Not Mentioned
[22]	1	None	NO	NO	Not Mentioned	Not Mentioned
[23]	n	None	NO	NO	Not Mentioned	Not Mentioned
[24]	n	None	NO	NO	1W	96.1%
[26]	1	None	NO	YES	1.6W	82%
[27]	1	None	NO	YES	7W	>80%
[28]	1	None	NO	YES	mW-level	>50%
[29]	1	YES	NO	NO	2.5mW	13%
[30]	n	None	YES	NO	25W	83.9%
This paper	n	XY plane 360°, Z plane 90°	YES	YES	85.92W	>79.6%

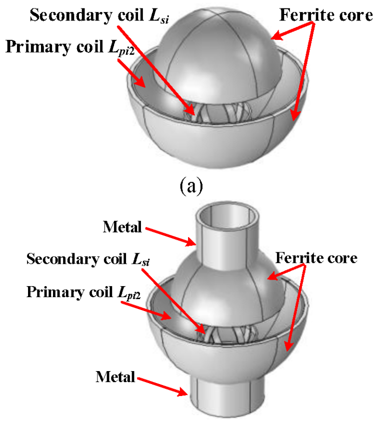

Fig. 16. COMSOL simulation models for comparison. (a) Without robot arm effect. (b) With robot arm effect.

If the primary coil is vertical to one of the secondary coils, there is no coupling between them. Under the condition of (28), this branch of the secondary coils will be short circuited, because the resistance of the coil is very small. Parallel connection cannot achieve the purpose of multidegree freedom to pick up power. Therefore, parallel connection is not suitable for this system.

B. Influence of the Robot Arm on the System

The metal material in the robot arm is the main cause of the robot arm effect. The metal in the robot arm may produce eddy current, which will affect the self-inductance, mutual inductance, and resistance of the coils. Therefore, the ferrite core is used to shield the magnetic field to reduce the influence of metal on the coil. Magnetic field analysis is carried out with COMSOL software, the simulation model is shown in Fig. 16, and the simulation results are shown in Tables XI and XII.

TABLE XI
WITHOUT ROBOT EFFECT

M_{rm} (μH)							L_{pi2}	L_{si}
θ=0°	θ=15°	θ=30°	θ=45°	θ=60°	θ=75°	θ=90°	(μH)	
4.67	5.83	6.49	6.57	6.10	5.17	4.48	83.1	6.2

TABLE XII
WITH ROBOT EFFECT

M_{rm} (μH)							L_{pi2}	L_{si}
θ=0°	θ=15°	θ=30°	θ=45°	θ=60°	θ=75°	θ=90°	(μH)	
4.65	5.81	6.47	6.55	6.08	5.15	4.47	84.2	6.5

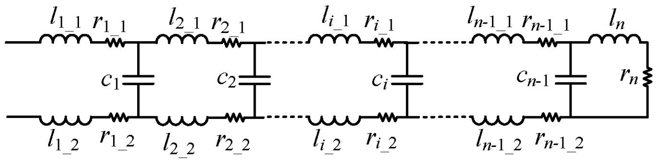

Fig. 17. Coil model considering stray capacitance.

In the proposed system, the operation frequency of 150 kHz is adopted. When stray capacitance is considered, the coil model is shown in Fig. 17.

As can be seen in Fig. 17, $c_1, c_2 \ldots c_{n\text{-}1}$ are the stray capacitances of the coil, and they are below PF level. The impedance of each stray capacitance can be expressed as

$$Z_{ci} = \frac{1}{j\omega c_i}. \tag{29}$$

Due to these capacitances are very small, the impedances of them are very large. Therefore, the capacitance branch is equivalent to an open circuit, and the influence of the stray capacitances on the system is little, then the equivalent circuit of the coil is shown in Fig. 18.

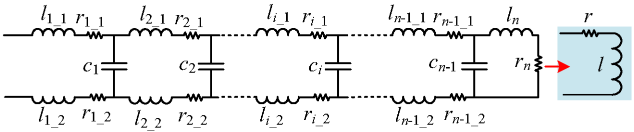

Fig. 18. Equivalent circuit of the coil.

In the equivalent circuit of the coil, l and r can be expressed as

$$l = \sum_{i=1}^{n-1} (l_{i\_1} + l_{i\_2}) + l_n \tag{30}$$

$$r = \sum_{i=1}^{n-1} (r_{i\_1} + r_{i\_2}) + r_n. \tag{31}$$

VIII. CONCLUSION

Aiming at WPT application on robot arm, a BM-WPT method with a special designed coupling mechanism is proposed in this article. In order to achieve stable mutual inductance when the coupling mechanism rotates, the primary and secondary coils adopt the bowl structure and the 3-D orthogonal ring coil arrangement, respectively. New coupling mechanism design reduces the sensitivity of the mutual inductance to the rotation of the coils. Furthermore, the power can be injected or output freely on each stage regardless of the direction in which the energy is transmitted. The simulation and experimental results have validated the effectiveness of the proposed WPT system.

REFERENCES

[1] R. Ito, Y. Sawahar, T. Ishizak, and I. Awai, “Construction of a secure wireless power transfer system,” in *Proc. IEEE Wireless Power Transfer Conf.*, 2015, pp. 1–4.

[2] L. Jialin, X. Wenxun, Z. Bo, Q. Dongyuan, and N. M. H. Carl, “Design of magnetic coupling resonant wireless charging system for cable tunnel inspection robot,” in *Proc. Wireless Power Transfer Conf.*, 2018, pp. 1–4.

[3] G. Yan, D. Ye, P. Zan, K. Wang, and G. Ma, “Micro-robot for endoscope based on wireless power transfer,” in *Proc. Int. Conf. Mechatronics Autom.*, 2007, pp. 3577–3581.

[4] D. Kim, J. Park, K. Kim, H. Ho Park, and S. Ahn, “Propulsion and control of implantable micro-robot based on wireless power transfer,” in *Proc. Wireless Power Transfer Conf.*, 2015, pp. 1–4.

[5] M. Sugino and T. Masamura, “The wireless power transfer systems using the Class E push-pull inverter for industrial robots,” in *Proc. Wireless Power Transfer Conf.*, 2017, pp. 1–3.

[6] I. K. Cho, S. M. Kim, J. I. Moon, J.-H. Yoon, S.-I. Jeon, and J.-I. Choi, “Wireless power transfer system for docent robot by using magnetic resonant coils,” in *Proc. 5th IEEE Int. Symp. Microw. Antenna, Propag. EMC Technol. Wireless Commun.*, 2013, pp. 251–254.

[7] A. Chan, “Development of long rail dynamic wireless power transfer for battery-free mobile robot,” in *Proc. Int. Conf. Power Electron. ECCE Asia*, 2019, pp. 1–6.

[8] R. Narayanamoorthi, A. V. Juliet, and C. Bharatiraja, “Frequency splitting-based wireless power transfer and simultaneous propulsion generation to multiple micro-robots,” *IEEE Sens. J.*, vol. 18, no. 13, pp. 5566–5575, Jul. 2018.

[9] D. Kim, J. Park, H. H. Park, and S. Ahn, “Generation of magnetic propulsion force and torque using wireless power transfer coil,” *IEEE Trans. Magn.*, vol. 51, no. 11, Nov. 2015, Art. no. 8600104.

[10] D. Kim, G. Hwang, J. Park, H. Ho Park, and S. Ahn, “High efficiency wireless power and force transfer for a micro-robot using a multi-axis AC/DC magnetic coil,” *IEEE Trans. Magn.*, vol. 53, no. 6, Jun. 2017, Art. no. 9401804.

[11] M. Ishizaki and A. Kurokawa, “Power transfer system combining wireless resonators and wired three-coil repeater,” *IEEE Int. Symp. Circuits Syst.*, 2019, pp. 1–4.

[12] W. Wang, X. Huang, S. Pan, and J. Guo, “Moving impedance matching analysis for three-coil wireless power transfer system in mid-range,” in *Proc. IEEE 5th Asia-Pacific Conf. Antennas Propag.*, 2016, pp. 429–430.

[13] I. Motoki and K. Atsushi, “Wireless power transfer system with long wired repeater,”in *Proc. IEEE 3rd Int. Conf. Integr. Circuits Microsyst.*, 2018, pp. 221–225.

[14] P. Kittisak, L. Titipong, C. Suramate, and A. Prayoot, “Area extension of a wireless battery charging system using multiple power repeater coil antennas,” in *Proc. Int. Conf. Intell. Green Building Smart Grid*, 2016, pp. 1–4.

[15] J. Zhao, X. Huang, and W. Wang, “Wireless power transfer with two-dimensional resonators,” *IEEE Trans. Magn* ., vol. 50, no. 1, pp. 1–4, Jan. 2014.

[16] W. Zhong and S. Hui, “Auxiliary circuits for power flow control in multifrequency wireless power transfer systems with multiple receivers,” *IEEE Trans. Power Electron.*, vol. 30, no. 10, pp. 5902–5910, Oct. 2015.

[17] Q. N. Minh*et al.*, “A study of coil orientations to enhance the transfer efficiency of a multi-repeater wireless power transmission system,” in *Proc. IEEE Asia-Pacific Microw. Conf.*, 2014, pp. 1354–1356.

[18] F. Zhang, S. A. Hackworth, W. Fu, and M. Sun, “Relay effect of wireless power transfer using strongly coupled magnetic resonances,” *IEEE Trans. Magn.*, vol. 47, no. 5, pp. 1478–1481, May 2011.

[19] Z. Wenxing, K. L. Chi, and S. Y. Ron Hui, “General analysis on the use of Tesla’s resonators in domino forms for wireless power transfer,” *IEEE Trans. Ind. Electron.*, vol. 60, no. 1, pp. 261–270, Jan. 2013.

[20] J. P. K. Sampath, A. Alphones, and D. M. Vilathgamuwa, “Optimization of wireless power transfer system with a repeater against load variations,” *IEEE Trans. Ind. Electron.*, vol. 64, no. 10, pp. 7800–7909, Oct. 2017.

[21] I. Masataka, U. Kazuhiro, and H. Eiji, “Automatic resonance frequency tuning method for repeater in resonant inductive coupling wireless power transfer systems,” in *Proc. Int. Power Electron. Conf.*, 2018, pp. 1610–1616.

[22] I. Masataka, U. Kazuhiro, and H. Eiji, “Impedance matching to maximize induced current in repeater of resonant inductive coupling wireless power transfer systems, in *Proc. Energy Convers. Congr. Expo.*, 2018, pp. 6194–6201.

[23] I. Masataka, O. Shoma, F. Keita, U. Kazuhiro, and E. Hiraki, “Improving robustness against variation in resonance frequency for repeater of resonant inductive coupling wireless power transfer systems,” in *Proc. Eur. Conf. Power Electron. Appl.*, 2018, pp. 1–9.

[24] B. Luo, S. Wu, and N. Zhou, “Flexible design method for multi-repeater wireless power transfer system based on coupled resonator bandpass filter model,” *IEEE Trans. Circuits Syst. I: Regular Papers*, vol. 61. no. 11, pp. 3288–3297, Nov. 2014.

[25] X. Dai, X. Li, Y. Li, and A. Patrick Hu, “Maximum efficiency tracking for wireless power transfer systems with dynamic coupling coefficient estimation,” *IEEE Trans. Power Electron.*, vol. 33. no. 6, pp. 5005–5015, Jun. 2018.

[26] M. N. Ruiz, D Vegas, J. R. Perez-Cisneros, and J. A. García, “GaN HEMT class-E rectifier for DC+AC power recovery,” in *Proc. IEEE/MTT-S Int. Microw. Symp.*, 2017, pp. 318–321.

[27] T. Reveyrand, I. Ramos, and Z. Popovic´. “Time-reversal duality of high-efficiency RF power amplifiers,” *Electron. Lett.*, vol. 48, no. 25, pp. 1607–1608, 2012.

[28] M. Del Prete, A. Costanzo, A. Georgiadis, A. Collado, D. Masotti, and Z. Popović, “A 2.45-GHz energy-autonomous wireless power relay node,” *IEEE Trans. Microw. Theory Techn.*, vol. 63, no. 12, pp. 4511–4520, Dec. 2015.

[29] A. Pacini, F. Benassi, D. Masotti, and A. Costanzo, “Design of a miniaturized omni-directional RF-to-dc IR-WPT,” in *Proc. IEEE Wireless Power Transfer Conf.*, 2018, pp. 1–4.

[30] C. Cheng *et al.*, “Load-independent wireless power transfer system for multiple loads over a long distance,” *IEEE Trans. Power Electron.*, vol. 34, no. 9, pp. 9279–9288, Sep. 2018.

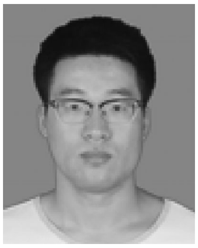

Jinde Wu received the B.S. degree from the College of Information Engineering, Taiyuan University of Technology, Taiyuan, China, in 2015. He is currently working toward the Ph.D. degree in control theory and control engineering with Chongqing University, Chongqing, China.

His current research interests include the bidirectional wireless power transfer and power electronics.

Xin Dai (Member, IEEE) received the B.S. degree in industrial automation from Yuzhou University, Chongqing, China, in 2000, and the Ph.D. degree in control theory and control engineering from the School of Automation, Chongqing University, Chongqing, China, in 2006.

In 2012, he was a Visiting Scholar with The University of Auckland, Auckland, New Zealand. He is currently working as a Professor with the School of Automation, Chongqing University. His current research interests include inductive power transfer technology and nonlinear dynamic behavior analysis of power electronics.

Ruozhong Gao received the B.S. and M.Sc. degrees in electrical engineering from the Taiyuan University of Technology, Taiyuan, China, in 2013 and 2017, respectively. He is currently working toward the Ph.D. degree in control theory and control engineering with Chongqing University, Chongqing, China.

His current research interests include the wireless power transfer and power electronics.

Jincheng Jiang received the B.S. degree from the College of Optoelectronic Engineering, Chongqing University of Posts and Telecommunications, Chongqing, China, in 2015. He is currently working toward the Ph.D. degree in control theory and control engineering with Chongqing University, Chongqing, China.

His current research interests include the dynamic wireless charging system and multiexcitation units wireless power transfer systems.